The Role of Oxygen Release from Li- and Mn-Rich Layered Oxides during the First Cycles Investigated by On-Line Electrochemical Mass Spectrometry

Benjamin Strehle,[a,*,z] Karin Kleiner,[a,*] Roland Jung,[a,*] Frederick Chesneau,[b] Manuel Mendez,[b] Hubert A. Gasteiger,[a,] and Michele Piana[a,***]**

[a]*Chair of Technical Electrochemistry, Department of Chemistry and Catalysis Research Center, Technische Universität München, D-85748 Garching, Germany*
[b]*BASF SE, GCN/EE - M311, D-67056 Ludwigshafen, Germany*

In the present work, the extent and the role of oxygen release during the first charge of lithium- and manganese-rich $Li_{1.17}[Ni_{0.22}Co_{0.12}Mn_{0.66}]_{0.83}O_2$ (also referred to as HE-NCM) was investigated with on-line electrochemical mass spectrometry (OEMS). HE-NCM shows a unique voltage plateau at around 4.5 V in the first charge, which is often attributed to a decomposition reaction of the Li-rich component Li_2MnO_3. For this so-called "activation", it has been hypothesized that the electrochemically inactive Li_2MnO_3 would convert into MnO_2 while lattice oxide ions are oxidized and released as O_2 (or even CO_2) from the host structure. However, qualitative and quantitative examination of the O_2 and CO_2 evolution during the first charge shows that the onset of both reactions is above the 4.5 V voltage plateau and that the amount of released oxygen is an order of magnitude too low to be consistent with the commonly assumed Li_2MnO_3 activation. Instead, the amount of released oxygen can be correlated to a structural rearrangement of the active material which occurs at the end of the first charge. In this process, oxygen depletion from the HE-NCM host structure leads to the formation of a spinel-like phase. This phase transformation is restricted to the near-surface region of the HE-NCM particles due to the poor mobility of oxide ions within the bulk. From the evolved amount of O_2 and CO_2, the thickness of the spinel-like surface layer was estimated to be on the order of ≈2–3 nm, in excellent agreement with previously reported (S)TEM data.

Manuscript submitted September 8, 2016; revised manuscript received November 21, 2016. Published January 5, 2017.

Since the discovery of the positive electrode material $LiCoO_2$ and its commercialization in the Li-ion technology by Sony in 1991,[1] analogous layered oxides ($LiMeO_2$, Me = Ni, Co, Mn, Al, etc.) were studied, aiming at higher intrinsic specific capacity, energy, stability, and lower costs.[2–7] Among others, $Li[Ni_{1/3}Co_{1/3}Mn_{1/3}]O_2$ (NCM-111) showed very interesting performances in terms of specific capacity and stability.[8,9] Recently, materials characterized by an increase of exploitable Li^+ charge drew a lot of attention.[10,11] These so-called Li-rich compounds result from the substitution of part of the transition metal ions by Li^+, in a structural arrangement closely related to the layered structure.[11–14]

Li_2MnO_3 (or $Li[Li_{1/3}Mn_{2/3}]O_2$) is the simplest structure in this category and crystallizes in the monoclinic system (space group *C2/m*), while the common $LiMeO_2$-based layered structures crystallize in the hexagonal system (space group *R-3m*).[11,13,14] The two structures are very close to each other despite this difference in symmetry, related simply to the Li^+ ordering in the transition metal sites. This similarity is evident in the structure of the Li-rich NCM $Li_{1+x}Me_{1-x}O_2$ (Me = Ni, Co, Mn), also referred to as high-energy NCM (HE-NCM), where the hexagonal symmetry of the layered structure is broken by the superstructure of Li^+ in the transition metal sites, shown by the superlattice reflections in the diffractograms.[15,16] This similarity makes the Li_2MnO_3 crystalline domains difficult to detect, for which typically the notation $x\ Li_2MnO_3 \bullet (1\text{-}x)\ LiMeO_2$ has been used.[14,17,18]

The higher lithium content of the HE-NCM material results in an increase in specific capacity and energy. Peculiar to this material is that the amount of lithium ions that can be deintercalated is higher than the possible increase in the valence of the transition metals. This was initially rationalized by the formation of an oxygen-deficient layered oxide throughout the bulk of the material, formed by oxygen loss during the first activation cycle.[19,20] Accordingly, subsequent on-line mass spectrometry studies demonstrated the evolution of O_2 during the first charge.[21–23] The observed oxygen release was commonly attributed to Li_2MnO_3 activation and assigned to a unique plateau in the first charge of HE-NCM.[24,25] In the proposed process, lattice O^{2-} anions are oxidized to O_2 and removed from the oxide bulk structure, while the initially inactive manganese becomes electrochemically active after the first activation charge. However, very recently, an alternative view has been proposed, namely the direct involvement of lattice oxide ions by oxygen redox in the reversible charge/discharge reaction.[26,27]

The present paper will critically discuss the extent and the role of oxygen release from the HE-NCM host structure during the first activation charge. By means of quantitative on-line electrochemical mass spectrometry (OEMS) analysis of the amount of evolved oxygen and the onset potential of oxygen evolution it can be clearly shown that the O_2 release does not take place during the 4.5 V plateau in the first charge (the so-called "activation"). Instead, we provide evidence that the O_2 release occurs due to a structural rearrangement, consistent with the formation of a spinel-like surface layer observed in several (S)TEM studies.[28–30] This hypothesis is in good agreement with the amount of oxygen observed in our study, which in turn would be too low for the previously proposed Li_2MnO_3 activation.[17,24]

Experimental

All experiments were conducted with $Li_{1.17}[Ni_{0.22}Co_{0.12}Mn_{0.66}]_{0.83}O_2$ (further on referred to as HE-NCM; BET >>1 $m^2\ g^{-1}$, BASF SE, Germany), which can also be written as $0.42\ Li_2MnO_3 \bullet 0.58\ Li[Ni_{0.38}Co_{0.21}Mn_{0.41}]O_2$. HE-NCM inks were prepared by mixing 96 wt% of HE-NCM, 2 wt% of Super C65 conductive carbon (Timcal, Switzerland), and 2 wt% of polyvinylidene fluoride binder (PVDF, Kynar HSV 900, Arkema, France) with *N*-methyl-2-pyrrolidone (NMP, anhydrous, 99.5%, Sigma-Aldrich, Germany) in a planetary orbital mixer (Thinky, USA) in several steps. In the case of standard electrodes for tests in Swagelok T-cells, the ink was coated onto an aluminum foil using a doctor blade at a wet-film thickness of 50 μm. For the OEMS measurements conducted in a specially designed cell,[31] the ink was coated on a steel mesh (SS316, aperture 26 μm, wire diameter 25 μm, The Mesh Company Ltd, UK) in order to allow access of the

*Electrochemical Society Student Member.
**Electrochemical Society Fellow.
***Electrochemical Society Member.
[z]E-mail: benjamin.strehle@tum.de

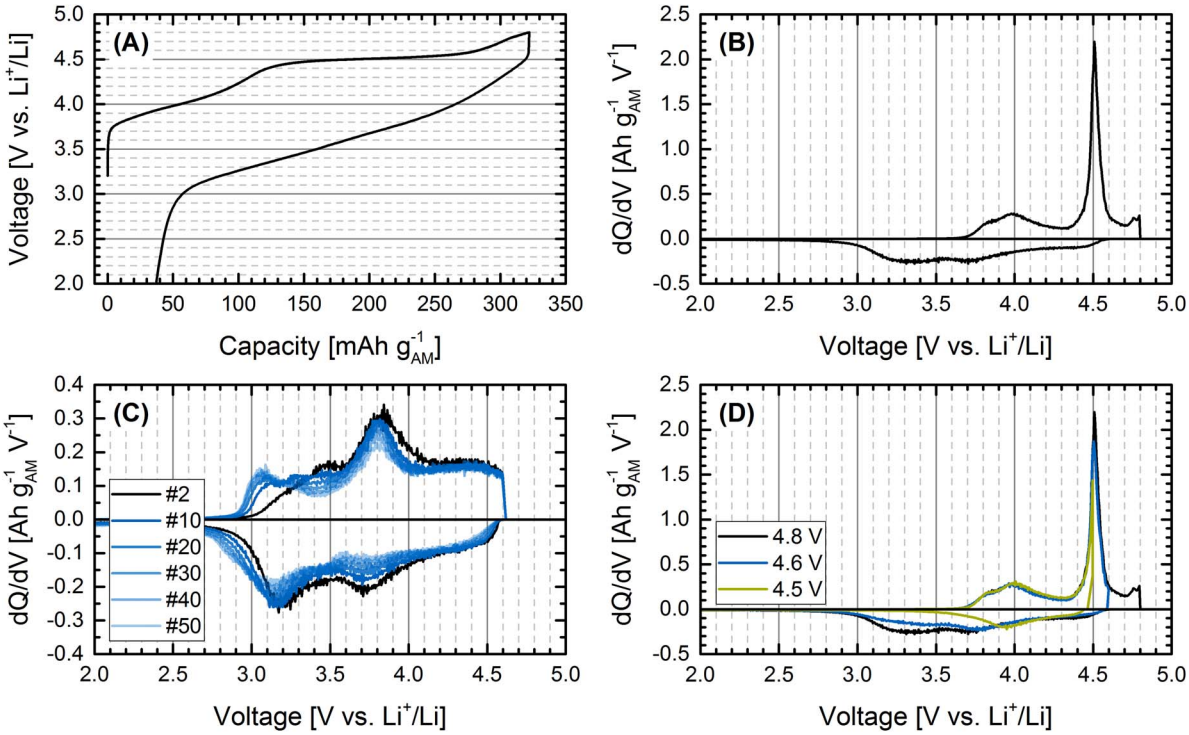

Figure 1. First cycle of HE-NCM (A) and the corresponding differential capacity (dQ/dV) plot (B). Panel C shows the differential capacity of the subsequent cycles. In panel D, the dQ/dV plot of the first cycle is shown for different upper voltage cutoffs, illustrating its influence on the discharge peaks. HE-NCM was cycled vs. metallic Li at a C-rate of C/10 and 25°C. In panel A-C, the first cycle was performed between 4.8 V and 2.0 V, while the upper cutoff voltage was 4.6 V for the subsequent cycles.

evolved gases to the capillary leading to the mass spectrometer.[32] The electrodes were punched out (loading/diameter: ≈4 mg_{AM} cm^{-2}/10 mm for T-cells and ≈10 mg_{AM} cm^{-2}/15 mm for OEMS cells), pressed for 20 s with 2.5 tons, and dried overnight at 120°C under dynamic vacuum. Swagelok T-cells were built using two glass fiber separators (glass microfiber filter, 691, VWR, Germany) and 120 µL LP57 electrolyte (1 M $LiPF_6$ in EC:EMC 3:7 by weight, <20 ppm H_2O, BASF SE). In contrast, OEMS cells were built using two porous polyolefin separators (H2013, Celgard, USA) and 100 µL LP57. Metallic lithium foil (thickness 0.45 mm, 99.9%, Rockwood Lithium, USA) was used as counter-electrode for all cells (diameter: 11 mm for T-cells and 17 mm for OEMS cells), except in one OEMS experiment, where a partially charged (delithiated) LFP counter-electrode with an areal capacity of 3.5 mAh cm^{-2} was used (from Custom Cells Itzehoe GmbH, Germany), which was charged at C/5 by 3.0 mAh cm^{-2}, corresponding to ca. $Li_{0.14}FePO_4$. Prior to cycling, the head space of the OEMS cells was purged for 2 min with argon to remove any gas traces from the glove box atmosphere. A 4 h OCV step was applied prior to starting the experiments. Conversion of the mass spectrometer currents to concentrations was done for O_2 and CO_2, using a calibration gas containing 2000 ppm of each gas in Ar (Westfalen AG, Germany). C-rates are defined based on a specific capacity of 300 mAh $g^{-1}{}_{AM}$ (AM ≡ cathode active material, HE-NCM in our case).

Results and Discussion

Electrochemical characterization.—HE-NCM shows a unique activation cycle with a plateau around 4.5 V in the first charge to 4.8 V (Figure 1A), yielding an overall capacity of ca. 320 mAh $g^{-1}{}_{AM}$, which is close to the theoretical capacity of the material of ca. 360 mAh $g^{-1}{}_{AM}$ (if one were to assume that all lithium could be extracted, based on $Li_{1.17}[Ni_{0.22}Co_{0.12}Mn_{0.66}]_{0.83}O_2$ with a molar mass of 86.8 g mol^{-1}). This can be seen more clearly in the differential capacity (dQ/dV) plot of the first charge/discharge cycle (Figure 1B), in which the activation plateau corresponds to a large peak at 4.5 V (HE-NCM vs. Li^+/Li). The presence of this peak is only observed in the first charge but not in the following cycles (Figure 1C). Depending on the voltage cutoff (before, on, or after the activation plateau), additional peaks appear at ca. 3.2 V and 3.7 V in the subsequent discharge cycles and at 3.0 V in the charge cycles (Figure 1C). The higher the end-of-charge voltage during the first activation cycle, the more pronounced are the additional peaks in the dQ/dV plot (Figure 1D). Apart from the electrochemical characterization, XRD patterns of the pristine material and after the first cycle are shown in the Supporting Information. The weak reflections between 9 and 12° are consistent with a two-phase rhombohedral-monoclinic system,[33] which clearly assign the material to the class of Li- and Mn-rich layered oxides (see Section 1 of the Supporting Information).

Li_2MnO_3 activation.—In the past, most authors have ascribed the origin of this so-called activation to the removal of oxygen from the bulk structure, leading to an oxygen-deficient bulk material.[17,19–21,24,25,34] Some of them attributed the activation of HE-NCM to the formation of delithiated MnO_2 according to Eq. 1,[17,24] which can be reversibly lithiated in the following discharge:

$$Li_2MnO_3 \rightarrow 2\,Li^+ + 2\,e^- + MnO_2 + 1/2\,O_2 \uparrow \qquad [1]$$

If following Eq. 1, the quantitative activation of Li_2MnO_3 in our material with the composition 0.42 Li_2MnO_3 • 0.58 $Li[Ni_{0.38}Co_{0.21}Mn_{0.41}]O_2$ (molar mass 104.8 g mol^{-1}) would lead to the release of ca. 2000 μmol_{O_2} $g^{-1}{}_{AM}$, corresponding to ca. 17% of all oxygen atoms in HE-NCM (calculation given in Section 2 of the Supporting Information). This requires transport of oxygen anions from the bulk of the material to the surface during activation, from where it could be released as molecular oxygen.

Gas evolution during first charge.—Figure 2 shows OEMS data obtained while charging HE-NCM vs. metallic Li at C/20 up to 4.8 V. Following the first constant current step (CC), one cell was held at open circuit voltage (OCV, black curve in Figure 2A) for 10 h, while

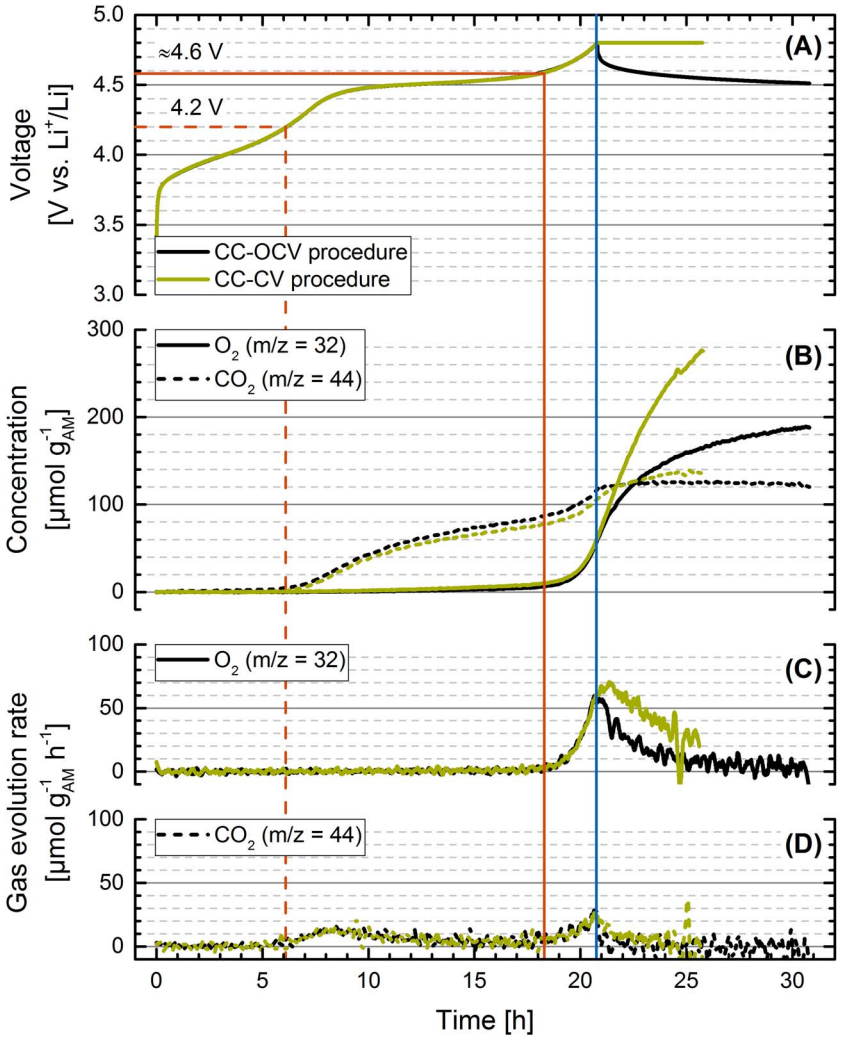

Figure 2. OEMS measurement of the first charge of HE-NCM vs. metallic Li to 4.8 V at C/20 and 25°C, followed by either an OCV step for 10 h (black curves) or a CV hold at 4.8 V for 5 h (green curves). Panel A shows the voltage curve vs. time (note that the curves are superimposed up to the upper cutoff voltage, i.e., up to ca. 21 h). Panel B illustrates the evolved amount of O_2 (solid curves) and CO_2 (dashed curves) in units of µmol g^{-1}_{AM}, whereas the O_2 and CO_2 evolution rates in units of µmol g^{-1}_{AM} h^{-1} are shown in the panels C and D, respectively. The dashed red lines indicate the initial onset potential of CO_2 evolution; the solid red lines indicate the onset potential of O_2 evolution (as well as the second onset potential for CO_2 evolution); the solid blue line marks the end of the CC charge at the cutoff voltage of 4.8 V.

another cell was held at 4.8 V in a constant voltage step (CV, green curve in Figure 2A) for 5 h, recording continuously the O_2 and CO_2 evolution in both cases (accumulated O_2 and CO_2 signals are shown in Figure 2B, while the evolution rates of O_2 and CO_2 are shown in Figure 2C and Figure 2D, respectively).

Starting with the CC-OCV experiment (black lines in Figure 2), the CO_2 evolution begins at 4.2 V (before the plateau), followed by a second increase at ≈4.6 V (after the plateau), which coincides with the onset potential for O_2 evolution. While the CO_2 release stops at the beginning of the OCV step, interestingly, the O_2 evolution goes on and does not complete within the measurement time. Let us first examine the evolution of CO_2. In agreement with Metzger et al.,[35] we attribute the initial CO_2 evolution starting at 4.2 V (marked by the dashed red lines in Figure 2) to the decomposition of carbonate impurities on the surface of the HE-NCM particles. The 4.2 V onset potential agrees with the Li_2CO_3 oxidation potential reported in the literature,[25,36,37] whereby essentially one CO_2 molecule per Li_2CO_3 is produced.[37] This first CO_2 evolution process continues up to a potential of ≈4.6 V (marked by the solid red lines in Figure 2), beyond which a second increase of the CO_2 evolution is observed. Note that the first process gradually levels off during the plateau, consistent with the consumption of an impurity which is only present in limited quantities. Up to ≈4.6 V, ≈80 μmol_{CO_2} g^{-1}_{AM} are evolved (Figure 2B), which for a 1:1 stoichiometric ratio between oxidized Li_2CO_3 and evolved CO_2 would correspond to a Li_2CO_3 content of ≈0.6 wt% (from: 80 μmol_{CO_2} g^{-1}_{AM} · 74 $g_{Li_2CO_3}$ $mol^{-1}_{Li_2CO_3}$). The calculated amount of Li_2CO_3 is to be expected on the HE-NCM particles (particularly in view of its rather high BET surface area[23]). This interpretation of the CO_2 signal is at variance with the mechanism proposed by Streich et al.[23] and by Luo et al.,[27] who concluded that the entire amount of CO_2 evolved during the initial charging of HE-NCM materials (i.e., including the CO_2 evolved between ≈4.2 and ≈4.6 V in their experiments) would originate from the attack of reactive oxygen species (e.g., superoxide radicals) released from the HE-NCM lattice on the electrolyte solvents. As evidence, Luo et al. noted the detection of $C^{16/18}O_2$ from their partially ^{18}O-labeled active material, but since their isotopic labeling process (heating the synthesized material in $^{18}O_2$-containing gas at 800°C) would also lead to the labeling of carbonate species, the formation of $C^{16/18}O_2$ can equally well be explained by the electrooxidation of Li_2CO_3 surface impurities. The latter are typically present in layered oxide materials.[38–40] However, the detection of $C^{16/18}O_2$ during the entire charging curve shows that the anodic oxidation of the electrolyte (without any involvement of the active material), which would release solely $C^{16/16}O_2$ in the experiment by Luo et al., is of minor importance for this class of materials. Thus, while we disagree with the interpretation by Streich et al.[23] and by Luo et al.[27] that the evolved CO_2 below ≈4.6 V originates from the reaction of the electrolyte with released lattice oxygen, we do believe that the second increase of the CO_2 evolution rate above 4.6 V, which coincides with the onset of O_2 evolution, is indeed caused by this reaction.

Next we will examine the O_2 evolution during the CC-OCV procedure. During the initial sloping region and during the high voltage plateau, i.e., at potentials below ≈4.6 V and a charge capacity of ≈280 mAh g^{-1}_{AM}, only minute amounts of O_2 are observed (less than 10 μmol_{O_2} g^{-1}_{AM}). This number could account for only

≈1 mAh g^{-1}_{AM} (assuming 4 electrons/O_2) and would thus be negligible compared to the overall charge capacity of ≈280 mAh g^{-1}_{AM}. Therefore, since the lattice oxygen evolution happens only after the plateau at 4.5 V, it cannot be correlated to the Li_2MnO_3 activation according to Eq. 1, as was done in some of the literature.[17,24] Only at potentials above ≈4.6 V, substantial O_2 evolution is observed, reaching a total amount of ≈60 μmol_{O_2} g^{-1}_{AM} once the positive voltage cutoff of 4.8 V is reached (see solid blue line in Figure 2). At this point, the charge capacity amounts to ≈310 mAh g^{-1}_{AM}, of which only ≈6.4 mAh g^{-1}_{AM} can be ascribed to the detected amount of O_2. The O_2 data may be compared to the study by Streich et al.,[23] who obtained 29 μmol_{O_2} g^{-1}_{AM} at a cutoff potential of 4.7 V, in excellent agreement with the ≈25 μmol_{O_2} g^{-1}_{AM} which we recorded at 4.7 V (Figure 2B). While the O_2 evolution rate (Figure 2C) is at its maximum at the positive voltage cutoff of 4.8 V, O_2 evolution continues even during the subsequent OCV period at a rate which decreases with decreasing potential. After 10 h of OCV, the potential decays to ≈4.5 V, at which point the total amount of O_2 approaches a value of ≈200 μmol_{O_2} g^{-1}_{AM} and the O_2 evolution gradually stops. Consequently, the total amount of evolved O_2 during the CC-OCV procedure amounts to only 10% of what would be predicted on the basis of Eq. 1 (i.e., of 2000 μmol_{O_2} g^{-1}_{AM}; see Section 2 of the Supporting Information). Note that the amount of O_2 dissolved in the electrolyte accounts to ca. 0.1% of the overall O_2 and is thus negligible compared to the gas phase which is detected by OEMS (calculation given in Section 3 of the Supporting Information). Even if we were to assume that all of the evolved CO_2 (≈120 μmol_{CO_2} g^{-1}_{AM}) would derive from the oxidation of the electrolyte by released lattice oxygen, as was suggested by Luo et al. (assuming the formation of 1 mol of CO_2 from 1 mol of released O_2),[27] only ≈16% of the evolved O_2 predicted by Eq. 1 would be released during the CC-OCV procedure. More likely, however, only ≈40 μmol_{CO_2} g^{-1}_{AM} derive from electrolyte oxidation by lattice oxygen (based on the above argument that CO_2 formed up to 4.6 V is due to Li_2CO_3 oxidation), so that the maximum amount of released oxygen (≈240 μmol g^{-1}_{AM}) amounts to ≈12% of what would be predicted by Eq. 1.

One remaining unresolved phenomenon in the CC-OCV data in Figure 2 is the fact that the CO_2 evolution stops very shortly after entering the OCV step (best seen by the CO_2 trace in Figure 2B), despite the fact that the amount of O_2 still increases by a factor of ≈3 (see O_2 trace in Figure 2B). This is clearly inconsistent with the above assumption that released lattice oxygen attacks the electrolyte solvents leading to CO_2 formation. As it seems to be required that charge passes the external circuit, one could hypothesize an (independent) oxidation step of the electrolyte which would be suppressed during OCV. Furthermore, as the released lattice oxygen species is not known, the absent CO_2 evolution might be explained by assuming that the oxidation of the electrolyte is largely triggered by superoxide radicals ($O_2^{\bullet -}$) rather than by molecular oxygen, which was proposed previously for alkyl carbonate-based electrolytes[41,42] as well as for the photo-assisted oxidation of organic dyes in aerated solutions.[43] At cathode potentials significantly above 3 V, superoxide radicals could only be formed by O_2 reduction at the lithium anode, where it might proceed as long as lithium is deposited (i.e., as long as a fresh lithium is being plated). Under this assumption, superoxide radicals to decompose the alkyl carbonates to CO_2 would be present during the CC step, but could not be supplied anymore during the OCV period. This will be discussed further when examining the gas evolution during the CC-CV charge.

Layered-to-spinel transformation.—Let us now summarize our observations so far: (i) almost no O_2 from the HE-NCM host structure is released during the activation plateau, (ii) the total amount of evolved gases is roughly one order of magnitude lower than what would be predicted based on Eq. 1, and (iii) the O_2 evolution continues during OCV, i.e., when no charge is passed. This provides strong evidence that the evolved O_2 is not related to the bulk oxidation of the Li_2MnO_3 phase according to Eq. 1. In contrast, the negligible amount of O_2 and the probably largely Li_2CO_3-derived CO_2 accumulated by the end of the voltage plateau (i.e., just below 4.6 V) suggests that the following oxygen release is associated with a structural rearrangement of the surface of the HE-NCM material, rather than being related to the electrochemically driven process described traditionally by Eq. 1. Such reactions are well-known from structurally related layered oxides and describe the chemical decomposition of Li_xMeO_2 into a spinel-like structure with the composition M'$_3$O$_4$ (M' = Me+Li), shown in Eq. 2.[44–46] This phase transformation is consistent with the observed phase reported in several (S)TEM studies from Li- and Mn-rich layered oxides (an overview is provided in Section 4 of the Supporting Information).[28–30,47–50] As the transition metal content in Li-rich materials is smaller than that for common layered oxides, the reaction is given in the generalized form for $Li_xMe_yO_2$. Especially in the case of Ni-rich materials,[51–55] the oxygen depletion of the near-surface region is a continuously ongoing process during cycling and/or at elevated temperatures, leading via the spinel structure to a rock-salt structure with the composition M'O (M' = Me+Li), described in Eq. 3.[44,45] The restriction of these reactions to the near-surface region can be rationalized by the low O^{2-} anion mobility within the bulk material at/near room temperature.

$$Li_xMe_yO_2 \rightarrow \frac{x+y}{3} Li_{3-\frac{3y}{x+y}} Me_{\frac{3y}{x+y}} O_4 + \frac{3-2(x+y)}{3} O_2 \uparrow, \quad \text{where } x \ll 1 \text{ and } y \leq 1 \qquad [2]$$

$$Li_xMe_yO_2 \rightarrow \frac{x+y}{3} Li_{3-\frac{3y}{x+y}} Me_{\frac{3y}{x+y}} O_4 + \frac{3-2(x+y)}{3} O_2 \uparrow$$
$$\rightarrow (x+y) Li_{1-\frac{y}{x+y}} Me_{\frac{y}{x+y}} O + \frac{2-(x+y)}{2} O_2 \uparrow \qquad [3]$$

In summary, Equations 2 and 3 present an alternative view to Eq. 1 of the oxygen evolution mechanism for HE-NCM materials during activation, assuming that oxygen is released by the conversion of a layered oxide into a spinel (or rock-salt) structure at high potentials. This picture would be by analogy with thermally induced phase transformations observed for charged layered oxide materials.[44–46,53]

In the second experiment shown in Figure 2, a C/20 activation charge to 4.8 V and then continued with a constant voltage step for 5 h was performed (see green curves). Up to the positive cutoff potential of 4.8 V, the voltage and gas evolution responses are identical with the foregoing experiment (compare green vs. black curves). The O_2 evolution rate during the 4.8 V hold period is substantially larger than during OCV (see black vs. green solid curves in Figure 2C), so that the total amount of evolved oxygen is larger at the end of the CV step (≈280 μmol_{O_2} g^{-1}_{AM} after 5 h CV compared to ≈200 μmol_{O_2} g^{-1}_{AM} after 10 h OCV, see Figure 2B). This seems to be at variance with our above assumption that the diffusion of O^{2-} anions within the bulk structure would limit the growth of the oxygen-depleted surface layer, i.e., that it would restrict the release of molecular oxygen to the near-surface region. However, since lithium deintercalation continues during the CV step (amounting to ≈20 mAh g^{-1}_{AM}), the oxide material becomes even more unstable, so that it is not unreasonable to assume that this would lead either to a slightly increased O^{2-} diffusion and/or a further conversion of the spinel layer to a rock-salt structure (Eq. 3). Both effects would be accompanied by further O_2 release. As the O_2 evolution rate during the CV step diminishes in a similar way than during OCV, we think that the oxygen depletion is still limited to the external part of the particles and does not affect the core of the particles. Note that Equation 2 and 3 describe the formation of the spinel (metal/oxygen ratio 3:4) and rock-salt structure (metal/oxygen ratio 1:1) with an ideal stoichiometry. However, it is also possible to reach stoichiometries in between in which the metal to oxygen ratio differs from the ideal case. Contrary to the CC-OCV experiment, the CO_2 evolution continues at low rate during most of the CV step, which would be consistent with an oxidation step of the alkyl carbonates or the continuous formation of superoxide radicals during lithium plating on the anode.

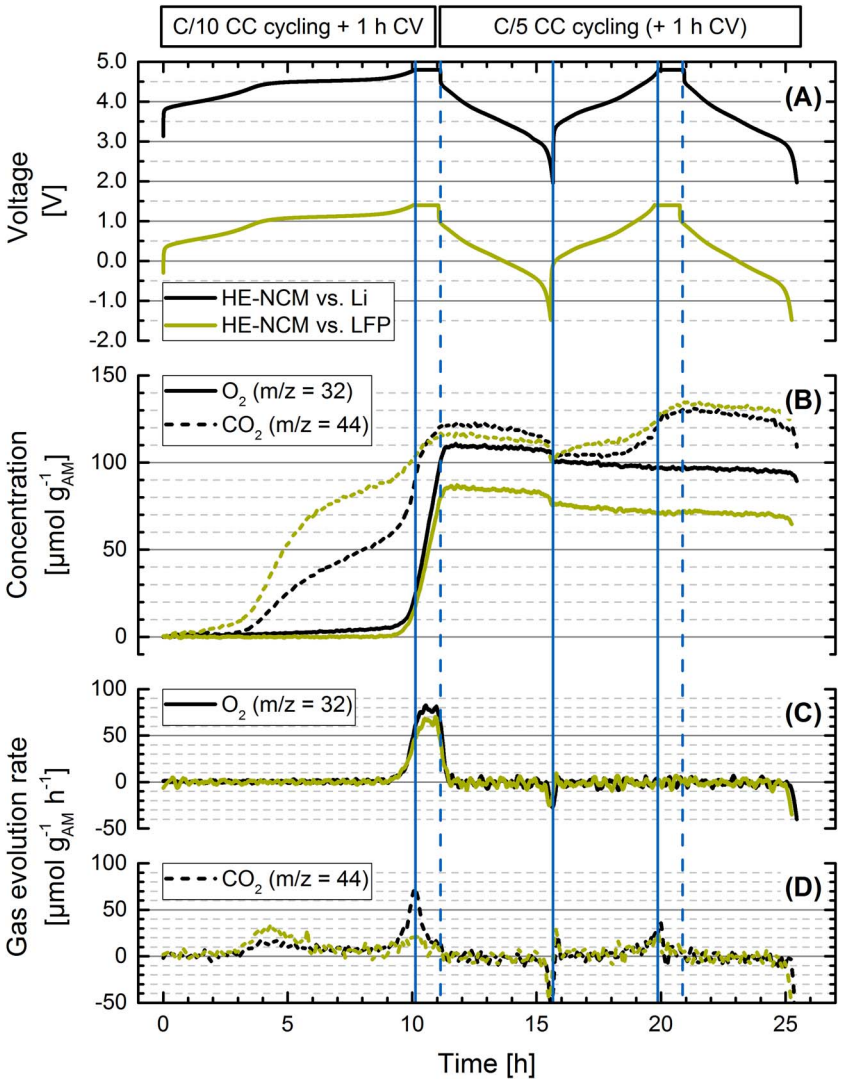

Figure 3. HE-NCM vs. Li (black curves) and HE-NCM vs. LFP (green curves), cycled at C/10 in the first charge and at C/5 in the subsequent discharge as well as the second cycle. Both measurements were performed at 25°C in the potential range of 2.0–4.8 V vs. Li^+/Li for the HE-NMC working-electrode, including a CV step of 1 h at the end of each CC charge. Panel A shows the voltage curves vs. time. Panel B illustrates the evolved amount of O_2 (solid curves) and CO_2 (dashed curves) in units of µmol g^{-1}_{AM}, whereas the O_2 and CO_2 evolution rates in units of µmol g^{-1}_{AM} h^{-1} are shown in the panels C and D, respectively. The blue solid lines indicate the end of the CC steps; the dotted blue lines show the end of the CV steps.

Gas evolution during the first two cycles.—After having examined the first activation charge, we now investigate whether O_2 release from the HE-NCM host structure also occurs in the second cycle or not (Figure 3). Therefore, using first the same electrode configuration as was used in Figure 2 (viz., HE-NCM vs. Li), we performed a C/10 charge to 4.8 V completed with a CV step of 1 h and followed by a C/5 discharge to 2.0 V, with a subsequent second cycle at C/5 (see black curves in Figure 3). Once the upper cutoff voltage is reached in this first charge at C/10, the amounts of evolved O_2 and CO_2 are lower than what we had observed at C/20 (≈25 µmol$_{O_2}$ g^{-1}_{AM} and ≈90 µmol$_{CO_2}$ g^{-1}_{AM} at C/10 vs. ≈60 µmol$_{O_2}$ g^{-1}_{AM} and ≈105 µmol$_{CO_2}$ g^{-1}_{AM} at C/20), which we ascribe to the slow kinetics of lattice oxygen release. However, at the end of the subsequent 1 h hold at 4.8 V, the amounts of evolved O_2 and CO_2 are essentially identical for first cycle activation at either C/10 or C/20 (≈110 µmol$_{O_2}$ g^{-1}_{AM} and ≈120 µmol$_{CO_2}$ g^{-1}_{AM} at C/10 + 1 h CV vs. ≈125 µmol$_{O_2}$ g^{-1}_{AM} and ≈120 µmol$_{CO_2}$ g^{-1}_{AM} at C/20 + 1 h CV). It is noteworthy that the O_2 evolution immediately stops upon switching from the CV step in the first cycle, during which O_2 is still being evolved, to the first discharge step. The rapidly vanishing O_2 evolution rate (Figure 3C) demonstrates that there is no delay between the O_2 evolution from the HE-NCM material and its detection in the OEMS. As the near-surface region is lithiated and thus stabilized first during discharge, the abrupt end of the O_2 evolution also shows that it must originate from the external part of the particles. Very surprising is the observation that there is no O_2 evolution during the second charge, even though the overall amount of evolved O_2 after the first charge at C/10 and 1 h hold at 4.8 V (≈110 µmol$_{O_2}$ g^{-1}_{AM}) is less than what was measured in the previous experiments with a C/20 charge and 5 h hold at 4.8 V (≈280 µmol$_{O_2}$ g^{-1}_{AM}). Consequently, any formed spinel-like surface layer in the former case should be thinner and further O_2 evolution in the second charge would be expected, contrary to what we and others[23] have observed. In order to explain this discrepancy, we hypothesize that the initially formed surface layer is modified during the first discharge, thereby preventing further oxygen release in subsequent charges. In addition, the change in the HE-NCM bulk structure upon the initial release of almost all of its lithium ions during activation (320 mAh g^{-1}_{AM} in the first charge vs. a theoretical maximum of ca. 360 mAh g^{-1}_{AM}) leads to different bulk thermodynamic properties, which might affect the oxygen release. Note that the overall capacity during the second charge decreases to ca. 275 mAh g^{-1}_{AM}. The OEMS measurement shows also a slight decrease in the O_2 and CO_2 signals once the potential decreases below 3.0 V at the end of discharge, which can be attributed to the formation of Li_2O_2 and Li_2CO_3 on the HE-NCM surface.[25,56] This newly formed Li_2CO_3 can then be oxidized in a subsequent charge, which we believe is the reason for the observed CO_2 evolution in the second charge, starting again at 4.2 V. This was already proposed previously.[56]

In order to ensure that no gaseous products are consumed on the Li counter-electrode, the same cycling procedure was applied to HE-NCM but using partially delithiated LFP as counter-electrode (green curves in Figure 3; see also in the experimental part). Neither O_2 nor CO_2 are expected to be reduced at the LFP potential.[57] Its potential was monitored in a T-cell with a Li reference-electrode to

Table I. Estimation of the molar fraction and thickness of the spinel-like surface layer for *Model A* (lattice oxygen-derived CO_2 only above ≈4.6 V) and *Model B* (CO_2 evolved prior to O_2 evolution at ≈4.6 V also due to the reaction with lattice oxygen), based on the gas evolution for the HE-NCM/Li cell data in Figure 3 (black lines). For CO_2, we assume that both oxygen atoms come from the lattice O^{2-} anions, as suggested by Luo et al.[27] The capacity is also derived from the gas evolution, assuming that four electrons are exchanged per gas molecule. For details see Section 5 and 6 of the Supporting Information.

		Model A (≥4.6 V)		*Model B* (≥4.2 V)	
Gas evolution	n [μmol g^{-1}_{AM}]	O_2	110	O_2	110
		CO_2	60	CO_2	120
Capacity ($4e^-/O_2$ & CO_2)	C_{spec} [mAh g^{-1}_{AM}]	18		25	
Fraction of spinel phase	x_{spinel} [mol.%]	5.7		7.7	
Spinel-like surface layer thickness	t_{spinel} [nm]	2.1		2.9	

determine the voltage cutoffs in the HE-NCM/LFP full-cell for the OEMS measurement (−1.45 V and 1.40 V selected as cell potential for the lower and upper voltage cutoffs). That the chosen cutoffs are reasonably comparable can be deduced from the close similarity of the charge/discharge curve features for the HE-NCM/Li and the HE-NCM/LFP cells (compare black and green curve in Figure 3A). The amount of evolved O_2 after the first cycle is slightly lower for the HE-NCM/LFP cell compared to the HE-NCM/Li cell (≈85 μmol_{O_2} g^{-1}_{AM} vs. ≈110 μmol_{O_2} g^{-1}_{AM}, respectively), but this might be due to small but finite differences in the upper voltage hold value. Regarding the CO_2 evolution, there are clear differences prior to the onset of O_2 evolution (reaching ≈90 μmol_{CO_2} g^{-1}_{AM} for HE-NCM/LFP vs. ≈60 μmol_{CO_2} g^{-1}_{AM} for HE-NCM/Li), which might be due to an inhomogeneous distribution of carbonate impurities among different electrodes. Overall, however, the differences in total gas evolution are not very large, so that any possible "cross-talk" effects between anode and cathode are either negligible or very similar.

Thickness of the spinel-like surface layer.—Assuming that the detected O_2 as well as the associated CO_2 obtained from Figure 3 derives from the formation of a near-surface spinel layer and not from the removal of oxygen from the bulk of the material, we will now estimate its thickness. The latter can be calculated by taking into account the amount of oxygen atoms which are released from the HE-NCM host structure according to Eq. 2. To perform this calculation, we will use two different models. *Model A*: We only consider the amount of gases evolved at a voltage higher than 4.6 V, i.e., once the onset of O_2 evolution is observed, which, without doubt, will derive from HE-NCM lattice oxygen. *Model B*: As some authors assume that the CO_2 observed prior to O_2 evolution (i.e., between 4.2 V and 4.6 V) originates from electrolyte oxidation by reaction with released lattice oxygen,[23,27] we will also provide an estimate for the near-surface layer thickness using the overall gas evolution (i.e., including the CO_2 evolution starting at 4.2 V), even though we believe that it is more likely due to the electrooxidation of Li_2CO_3 impurities. These two models will now be applied to the HE-NCM/Li cell data shown in Figure 3 (black lines). The formation of a spinel structure (M'_3O_4, M' = Me+Li) at 4.6 V, corresponding to a charge capacity of ≈275 mAh g^{-1}_{AM} at C/10, can be written as follows (see Supporting Information for more details):

$$Li_{0.28}Me_{0.83}O_2 \rightarrow 0.37\ Li_{0.76}Me_{2.24}O_4 + 0.26\ O_2 \uparrow \quad [4]$$

Comparing the results in Table I, the difference between the two models is less than 1 nm which is reasonably small compared to the estimated average HE-NCM particle radius of ≈110 nm (see Section 6 of the Supporting Information) and based on the approximations used for this calculation. Nevertheless, the estimated thickness of ≈2–3 nm for the spinel-like phase is in excellent agreement with recent (S)TEM results, which propose also a 2–3 nm thick surface layer formed during the first cycle.[28–30] As already mentioned in the discussion of Figure 2, it is not possible to determine whether the transformation of the near-surface region stops at the spinel structure (as described in Eq. 2) and to what extent it may proceed all the way to the rock-salt structure (as described in Eq. 3). In the latter case, the estimated thickness of the near-surface layer would be smaller by a factor of ca. 2. The overall maximum estimated capacity of ≈25 mAh g^{-1}_{AM} is five times lower than the capacity provided by HE-NCM during the plateau. However, the gas evolution does not occur during the plateau but mostly after plateau at potentials of 4.6 V and above, proceeding even if HE-NCM is hold at open circuit potential after the first charge.

Conclusions

In the present work, we show the gas evolution of HE-NCM during the first two cycles using OEMS. The gas evolution can be divided into a CO_2 evolution starting at 4.2 V and ending before 4.6 V, followed by a second CO_2 production starting at 4.6 V after the activation plateau and coinciding with the onset of the evolution of O_2. In agreement with the literature[25,35,37,56] and according to the use of a Li excess in HE-NCM synthesis, we attribute the CO_2 evolution at low voltages mainly to the electrooxidation of Li_2CO_3 impurities, while the O_2 and CO_2 evolution at voltages higher than 4.6 V are both attributed to oxygen evolved from the HE-NCM lattice. We exclude any possible gas consumption on the Li counter-electrode by comparing the results obtained with LFP as counter-electrode. The maximum recorded gas evolution due to lattice oxygen upon extended potential hold at 4.8 V (see CC-CV experiment in Figure 2), ≈420 μmol g^{-1}_{AM} (assuming that CO_2 evolution at low potentials is due to electrolyte oxidation by released lattice oxygen) or ≈340 μmol g^{-1}_{AM} (assuming that CO_2 evolution at low potentials is due to the oxidation of Li_2CO_3 impurities), is, in any case, at least 5-fold lower than what would be expected for the so-called Li_2MnO_3 activation (2000 μmol g^{-1}_{AM}) assumed in the literature.[17,24] This led us to propose an alternative reaction to the Li_2MnO_3 activation, namely, the formation of a spinel-like near-surface structure analogous to the known structural rearrangements in layered oxides. From the amount of evolved gases, we estimated the thickness of such a spinel-like surface layer on the HE-NCM particles to be on the order of ≈2–3 nm, in excellent agreement with previously observed (S)TEM data.[28–30]

Acknowledgments

The authors gratefully acknowledge BASF SE for financial support of this research through the framework of its Scientific Network on Electrochemistry and Batteries. R.J. thanks BMW AG for funding.

References

1. K. Mizushima, P. C. Jones, P. J. Wiseman, and J. B. Goodenough, *Mater. Res. Bull.*, **15**, 783 (1980).
2. C. Delmas and I. Saadoune, *Solid State Ionics*, **53–56**, 370 (1992).
3. T. Ohzuku, A. Ueda, and M. Kouguchi, *J. Electrochem. Soc.*, **142**, 4033 (1995).
4. T. Ohzuku and Y. Makimura, *Chem. Lett.*, **30**, 744 (2001).
5. J. S. Weaving, F. Coowar, D. A. Teagle, J. Cullen, V. Dass, P. Bindin, R. Green, and W. J. Macklin, *J. Power Sources*, **97–98**, 733 (2001).
6. Z. Lu, D. D. MacNeil, and J. R. Dahn, *Electrochem. Solid-State Lett.*, **4**, A200 (2001).
7. F. Zhou, X. Zhao, and J. R. Dahn, *J. Electrochem. Soc.*, **156**, A343 (2009).
8. I. Belharouak, Y.-K. Sun, J. Liu, and K. Amine, *J. Power Sources*, **123**, 247 (2003).
9. J. Choi and A. Manthiram, *J. Electrochem. Soc.*, **152**, A1714 (2005).
10. Z. Lu and J. R. Dahn, *J. Electrochem. Soc.*, **149**, A1454 (2002).
11. Z. Lu, L. Y. Beaulieu, R. A. Donaberger, C. L. Thomas, and J. R. Dahn, *J. Electrochem. Soc.*, **149**, A778 (2002).

12. Y. S. Meng, G. Ceder, C. P. Grey, W. S. Yoon, M. Jiang, J. Bréger, and Y. Shao-Horn, *Chem. Mater.*, **17**, 2386 (2005).
13. N. Tran, L. Croguennec, C. Labrugère, C. Jordy, P. Biensan, and C. Delmas, *J. Electrochem. Soc.*, **153**, A261 (2006).
14. M. M. Thackeray, S.-H. Kang, C. S. Johnson, J. T. Vaughey, R. Benedek, and S. A. Hackney, *J. Mater. Chem.*, **17**, 3112 (2007).
15. J. Bréger, M. Jiang, N. Dupré, Y. S. Meng, Y. Shao-Horn, G. Ceder, and C. P. Grey, *J. Solid State Chem.*, **178**, 2575 (2005).
16. K. A. Jarvis, Z. Deng, L. F. Allard, A. Manthiram, and P. J. Ferreira, *Chem. Mater.*, **23**, 3614 (2011).
17. J.-S. Kim, C. S. Johnson, J. T. Vaughey, M. M. Thackeray, S. A. Hackney, W. Yoon, and C. P. Grey, *Chem. Mater.*, **16**, 1996 (2004).
18. M. M. Thackeray, C. S. Johnson, J. T. Vaughey, N. Li, and S. A. Hackney, *J. Mater. Chem.*, **15**, 2257 (2005).
19. Z. Lu and J. R. Dahn, *J. Electrochem. Soc.*, **149**, A815 (2002).
20. N. Tran, L. Croguennec, M. Ménétrier, F. Weill, P. Biensan, C. Jordy, and C. Delmas, *Chem. Mater.*, **20**, 4815 (2008).
21. A. R. Armstrong, M. Holzapfel, P. Novák, C. S. Johnson, S.-H. Kang, M. M. Thackeray, and P. G. Bruce, *J. Am. Chem. Soc.*, **128**, 8694 (2006).
22. F. La Mantia, F. Rosciano, N. Tran, and P. Novák, *J. Appl. Electrochem.*, **38**, 893 (2008).
23. D. Streich, A. Guéguen, M. Mendez, F. Chesneau, P. Novák, and E. J. Berg, *J. Electrochem. Soc.*, **163**, A964 (2016).
24. H. Yu, H. Kim, Y. Wang, P. He, D. Asakura, Y. Nakamura, and H. Zhou, *Phys. Chem. Chem. Phys.*, **14**, 6584 (2012).
25. N. Yabuuchi, K. Yoshii, S.-T. Myung, I. Nakai, and S. Komaba, *J. Am. Chem. Soc.*, **133**, 4404 (2011).
26. H. Koga, L. Croguennec, M. Ménétrier, P. Mannessiez, F. Weill, C. Delmas, and S. Belin, *J. Phys. Chem. C*, **118**, 5700 (2014).
27. K. Luo, M. R. Roberts, R. Hao, N. Guerrini, D. M. Pickup, Y.-S. Liu, K. Edström, J. Guo, A. V. Chadwick, L. C. Duda, and P. G. Bruce, *Nat. Chem.*, **8**, 684 (2016).
28. A. Boulineau, L. Simonin, J.-F. Colin, E. Canévet, L. Daniel, and S. Patoux, *Chem. Mater.*, **24**, 3558 (2012).
29. A. Boulineau, L. Simonin, J.-F. Colin, C. Bourbon, and S. Patoux, *Nano Lett.*, **13**, 3857 (2013).
30. C. Genevois, H. Koga, L. Croguennec, M. Ménétrier, C. Delmas, and F. Weill, *J. Phys. Chem. C*, **119**, 75 (2015).
31. S. Meini, M. Piana, N. Tsiouvaras, A. Garsuch, and H. A. Gasteiger, *Electrochem. Solid-State Lett.*, **15**, A45 (2012).
32. N. Tsiouvaras, S. Meini, I. Buchberger, and H. A. Gasteiger, *J. Electrochem. Soc.*, **160**, A471 (2013).
33. F. Amalraj, M. Talianker, B. Markovsky, D. Sharon, L. Burlaka, G. Shafir, E. Zinigrad, O. Haik, D. Aurbach, J. Lampert, M. Schulz-Dobrick, and A. Garsuch, *J. Electrochem. Soc.*, **160**, A324 (2012).
34. J. R. Croy, K. G. Gallagher, M. Balasubramanian, Z. Chen, Y. Ren, D. Kim, S.-H. Kang, D. W. Dees, and M. M. Thackeray, *J. Phys. Chem. C*, **117**, 6525 (2013).
35. M. Metzger, B. Strehle, S. Solchenbach, and H. A. Gasteiger, *J. Electrochem. Soc.*, **163**, A798 (2016).
36. B. D. McCloskey, D. S. Bethune, R. M. Shelby, G. Girishkumar, and A. C. Luntz, *J. Phys. Chem. Lett.*, **2**, 1161 (2011).
37. S. Meini, N. Tsiouvaras, K. U. Schwenke, M. Piana, H. Beyer, L. Lange, and H. A. Gasteiger, *Phys. Chem. Chem. Phys.*, **15**, 11478 (2013).
38. K. Matsumoto, R. Kuzuo, K. Takeya, and A. Yamanaka, *J. Power Sources*, **81–82**, 558 (1999).
39. N. Mijung, Y. Lee, and J. Cho, *J. Electrochem. Soc.*, **153**, A935 (2006).
40. S.-W. Lee, H. Kim, M.-S. Kim, H.-C. Youn, K. Kang, B.-W. Cho, K. C. Roh, and K.-B. Kim, *J. Power Sources*, **315**, 261 (2016).
41. S. A. Freunberger, Y. Chen, Z. Peng, J. M. Griffin, L. J. Hardwick, F. Bardé, P. Novák, and P. G. Bruce, *J. Am. Chem. Soc.*, **133**, 8040 (2011).
42. V. S. Bryantsev, V. Giordani, W. Walker, M. Blanco, S. Zecevic, K. Sasaki, J. Uddin, D. Addison, and G. V. Chase, *J. Phys. Chem. A*, **115**, 12399 (2011).
43. M. Stylidi, D. I. Kondarides, and X. E. Verykios, *Appl. Catal. B Environ.*, **47**, 189 (2004).
44. N. Yabuuchi, Y.-T. Kim, H. H. Li, and Y. Shao-Horn, *Chem. Mater.*, **20**, 4936 (2008).
45. S.-M. Bak, K.-W. Nam, W. Chang, X. Yu, E. Hu, S. Hwang, E. A. Stach, K.-B. Kim, K. Y. Chung, and X.-Q. Yang, *Chem. Mater.*, **25**, 337 (2013).
46. S.-M. Bak, E. Hu, Y. Zhou, X. Yu, S. D. Senanayake, S.-J. Cho, K.-B. Kim, K. Y. Chung, X.-Q. Yang, and K.-W. Nam, *ACS Appl. Mater. Interfaces*, **6**, 22594 (2014).
47. A. K. Shukla, Q. M. Ramasse, C. Ophus, H. Duncan, F. Hage, and G. Chen, *Nat. Commun.*, **6**, 8711 (2015).
48. B. Qiu, M. Zhang, L. Wu, J. Wang, Y. Xia, D. Qian, H. Liu, S. Hy, Y. Chen, K. An, Y. Zhu, Z. Liu, and Y. S. Meng, *Nat. Commun.*, **7**, 12108 (2016).
49. H. Koga, L. Croguennec, P. Mannessiez, M. Ménétrier, F. Weill, L. Bourgeois, M. Duttine, E. Suard, and C. Delmas, *J. Phys. Chem. C*, **116**, 13497 (2015).
50. P. Yan, A. Nie, J. Zheng, Y. Zhou, D. Lu, X. Zhang, R. Xu, I. Belharouak, X. Zu, J. Xiao, K. Amine, J. Liu, F. Gao, R. Shahbazian-Yassar, J.-G. Zhang, and C.-M. Wang, *Nano Lett.*, **15**, 514 (2015).
51. D. P. Abraham, R. D. Twesten, M. Balasubramanian, I. Petrov, J. McBreen, and K. Amine, *Electrochem. Commun.*, **4**, 620 (2002).
52. S. Muto, Y. Sasano, K. Tatsumi, T. Sasaki, K. Horibuchi, Y. Takeuchi, and Y. Ukyo, *J. Electrochem. Soc.*, **156**, A371 (2009).
53. L. Wu, K.-W. Nam, X. Wang, Y. Zhou, J.-C. Zheng, X.-Q. Yang, and Y. Zhu, *Chem. Mater.*, **23**, 3953 (2011).
54. S.-K. Jung, H. Gwon, J. Hong, K.-Y. Park, D.-H. Seo, H. Kim, J. Hyun, W. Yang, and K. Kang, *Adv. Energy Mater.*, **4**, 1300787 (2014).
55. R. Jung, M. Metzger, F. Maglia, C. Stinner, and H. A. Gasteiger, Manuscript in preparation.
56. J. Hong, H. D. Lim, M. Lee, S. W. Kim, H. Kim, S. T. Oh, G. C. Chung, and K. Kang, *Chem. Mater.*, **24**, 2692 (2012).
57. A. Guéguen, D. Streich, M. He, M. Mendez, F. F. Chesneau, P. Novák, and E. J. Berg, *J. Electrochem. Soc.*, **163**, A1095 (2016).